RSC Advances

PAPER

View Article Online
View Journal | View Issue

Cite this: *RSC Adv.*, 2024, **14**, 2016

Effect of injectable calcium alginate–amelogenin hydrogel on macrophage polarization and promotion of jawbone osteogenesis†

Tingting Zhao,‡[a] Luyuan Chen,‡[b] Chengcheng Yu,‡[c] Gang He,[c] Huajun Lin,[c] Hongxun Sang,[e] Zhihui Chen,*[b] Yonglong Hong,*[c] Wen Sui*[d] and Jianjiang Zhao*[a]

Due to persistent inflammation and limited osteogenesis, jawbone defects present a considerable challenge in regenerative medicine. Amelogenin, a major protein constituent of the developing enamel matrix, demonstrates promising capabilities in inducing regeneration of periodontal supporting tissues and exerting immunomodulatory effects. These properties render it a potential therapeutic agent for enhancing jawbone osteogenesis. Nevertheless, its clinical application is hindered by the limitations of monotherapy and its rapid release characteristics, which compromise its efficacy and delivery efficiency. In this context, calcium alginate hydrogel, recognized for its superior physicochemical properties and biocompatibility, emerges as a candidate for developing a synergistic bioengineered drug delivery system. This study describes the synthesis of an injectable calcium amelogenin/calcium alginate hydrogel using calcium alginate loaded with amelogenin. We comprehensively investigated its physical properties, its role in modulating the immunological environment conducive to bone healing, and its osteogenic efficacy in areas of jawbone defects. Our experimental findings indicate that this synthesized composite hydrogel possesses desirable mechanical properties such as injectability, biocompatibility, and biodegradability. Furthermore, it facilitates jawbone formation by regulating the bone-healing microenvironment and directly inducing osteogenesis. This research provides novel insights into the development of bone-tissue regeneration materials, potentially advancing their clinical application.

Received 26th July 2023
Accepted 14th December 2023

DOI: 10.1039/d3ra05046g

rsc.li/rsc-advances

Introduction

Trauma, severe periodontal disease, malignant tumor metastasis, resorption of alveolar bone due to tumor resection, congenital cranial malformation, and osteonecrosis of the jaw contribute to maxillofacial dysfunction, bone-tissue deficiency, bone-tissue loss, and aesthetic deformity.[1] These conditions can seriously affect masticatory efficiency and quality of life. In cases necessitating maxillofacial bone-tissue restoration, particularly when the bone defects exceed the threshold for autologous repair, rapid healing of the bone tissue is not feasible. This scenario mandates the application of specialized biological tissue regenerative scaffolds to facilitate repair.[2,3] Researchers using renewable materials to restore defective or resorbed periodontal bone tissue have found that the materials are highly susceptible to severe rejection, disease transmission, and excessive trauma to the implant area.[4,5] The immune response of the host to the implant material plays a crucial role in the variance of osteogenic activity *in vivo* and *in vitro*. In this context, "third-generation bone replacement materials" are defined as biologically active and biodegradable biomaterials that not only induce new bone formation but also degrade the implant in a balanced manner; this is referred to as the "trade-off" type. The development of such materials, which can fill defects, degrade progressively, and guide bone regeneration, has garnered increasing attention in recent years. Moreover, improving osteogenic repair efficacy requires understanding the influence of the bone immune microenvironment and the direct effect of the material on the osteogenic differentiation of osteogenic-related cells. Therefore, new materials that can regulate the immune microenvironment to promote osteogenesis are urgently required.

[a]*Shenzhen Stomatological Hospital, Southern Medical University, 1092 Jianshe Road, Luohu District, Shenzhen, Guangdong 518001, China. E-mail: zjj2521@sina.com*

[b]*Stomatology Center, Shenzhen Hospital, Southern Medical University, 1333 Xinhu Road, Baoan District, Shenzhen, Guangdong 510086, China. E-mail: sophinaczh@outlook.com*

[c]*Department of Maxillofacial Surgery, Shenzhen Hospital, Southern Medical University, 1333 Xinhu Road, Baoan District, Shenzhen, Guangdong 510086, China. E-mail: ylhong93@163.com*

[d]*College of Stomatology, Shenzhen Technology University, 3002 Lantian Road, Pingshan District, Shenzhen, Guangdong 518118, China. E-mail: wens27@163.com*

[e]*Shenzhen Key Laboratory of Digital Surgical 3D Printing, Department of Orthopaedics, Shenzhen Hospital, Southern Medical University, 1333 Xinhu Road, Baoan District, Shenzhen, Guangdong , 510086, China*

† Electronic supplementary information (ESI) available. See DOI: https://doi.org/10.1039/d3ra05046g

‡ These authors contributed equally to this work.

Macrophages are activated by the synergistic effects of bioactive factors and the tissue microenvironment in various pathways; the activation of the classical pathway (M1) and alternative pathway (M2) is called polarization. M2 macrophages secrete interleukin-4, interleukin-10, and other anti-inflammatory factors, as well as process tissue necrosis debris, to maintain tissue microenvironment homeostasis.[6] M2 macrophages also produce a large number of growth factors and chemokines related to bone healing, contributing to the homing and migration of bone marrow mesenchymal stem cells (BMSCs) and bone healing.

Amelogenin (AM) is an essential component of enamel matrix proteins, and current findings suggest that it can induce periodontal support tissue regeneration;[7–9] however, studies on its mechanism of action are rare. Yamamichi *et al.* showed that AM could induce M2 polarization and promote periodontal tissue healing and regeneration.[10] AMs are highly susceptible to enzymatic degradation by cathepsin K and matrix metalloproteinase 20 (MMP20) *in vivo*;[11,12] they cannot persist in the defective areas of periodontal tissues long enough to match the ratio of periodontal tissue regeneration. Therefore, there is a need to compound AM within a slow-release drug delivery system to allow long-term release and produce the corresponding effect of inducing periodontal tissue regeneration.

Biological scaffold materials should be biocompatible and biodegradable, possess good mechanical properties, and be able to promote new bone formation.[13–15] Natural polymeric materials enhance angiogenesis, promote osteogenesis, and induce tissue repair;[16] among them, calcium alginate (CA), a natural polysaccharide material, has become a preferred base material for composites because of its biocompatibility and efficient drug-carrying ability.

This study designed an injectable calcium alginate–amelogenin hydrogel (CA + AM), which possesses good biosafety, bone-tissue regeneration induction, and macrophage-directed polarization ability and exhibits great potential for promoting bone-tissue regeneration and tissue repair (Scheme 1).

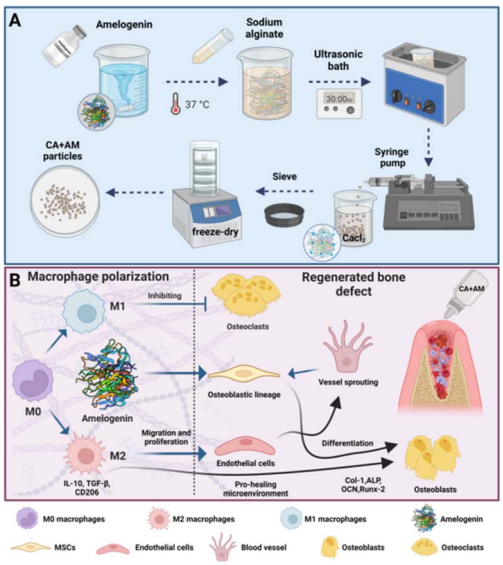

Scheme 1 Schematic illustration for the preparation and application of particles. (A) Chemical structure of the CA + AM particles. (B) Schematic illustration depicting the mechanism of particles used in extraction wounds to promote bone regeneration. Created at https://BioRender.com.

Experimental

Materials

Amelogenin (AM, SAB, USA); sodium alginate (Sigma, USA); calcium chloride (Sigma, USA); phosphate-buffered saline (PBS, Nacalai tesque, USA); Dulbecco's modified eagle medium (Gibco, USA); mouse macrophage colony aggregation factor (Peprotech, USA); Alizarin Red S (ARS) staining solution (Leagene, China); lipopolysaccharide (Sigma, USA); polyvinylidene difluoride (PVDF) membrane (Millipore, USA); Cell Counting Kit-8 (CCK-8); cell proliferation and toxicity assay kit (Meilunbio, China); alkaline phosphatase (ALP) assay kit (Beyotime, China); reverse transcription kit (EZBioscience, China); RIPA lysis buffer (Biosharp, Beijing, China); BCA kit (Leagene, Beijing, China); chemiluminescence assay kit (Enzyme, China); EDTA (Guangzhou Chemical Factory, China); 4% paraformaldehyde solution (Guangzhou Chemical Factory, China); hematoxylin-eosin stain (Ziker Bioziker, China).

Preparation of CA + AM

The CA was prepared *via* ionic cross-linking. First, 25 mg mL^{-1} of sodium alginate solution was added to deionized water and placed in an oven at 37 °C for 12 h to eliminate air bubbles. Then, the solution was injected into a 1% calcium chloride solution using a 5 mL disposable syringe and soaked in the calcium chloride solution for 12 h to obtain the final product, CA hydrogel. Finally, the solution was removed and lyophilized for 24 h.

Exactly 30 μg mL^{-1} of AM was dispersed with sodium alginate solution using an ultrasonic water bath shaker and placed in an oven at 37 °C for 12 h to eliminate air bubbles. Next, the solution was injected into a 1% calcium chloride solution using a 5 mL disposable syringe and soaked in the calcium chloride solution for 12 h to obtain the final product, which was then removed and lyophilized for 24 h.

Scanning electron microscopy (SEM) and optical microscopy analyses

SEM was used to determine whether the pre- and post-structures of the CA composite AM were consistent. Field emission SEM (JSM6700F; JEOL, Japan) was used to observe the experimental samples at low voltages using the principle of secondary electron imaging. First, the samples were aligned with liquid nitrogen for brittle fracture treatment and fixed on a conductive adhesive, followed by gold spraying. Next, the sample morphology was observed using SEM; multiple points were selected for each experimental sample for multidirectional

observations during the observation process. Optical microscopy was used to observe and analyze the structures and morphologies of the prepared sodium alginate samples.

Swelling ratio measurement

The swelling ratio of CA + AM was tested using PBS (pH 7.4) to simulate the liquid environment in the organism. First, regularly shaped CA + AM ($n = 5$) was prepared using a cylindrical mold (5 mm height and 10 mm diameter). Next, the target hydrogels were weighed (initial weight, W_0) and placed in 50 mL of PBS. The PBS containing the target hydrogels was placed in a constant temperature (37 °C) – shaking incubator. Simultaneously, the target hydrogels were removed and weighed (W_t). The swelling ratio was calculated as follows (eqn (1)):

$$\text{Swelling ratio (\%)} = (W_t - W_0)/W_0 \times 100\%, \quad (1)$$

Determination of degradation ratio

Prepared samples of CA and CA + AM of the same weight, 3000 mg, were transferred into PBS solution and placed in a thermostatic shaker at 37 °C. The dry weight was then measured, and the degradation ratio was calculated. The dry weight of the material was measured weekly for 6 weeks. Each set of data was recorded in detail, and the dry weight loss ratio of the experimental gel samples was calculated according to the following formula (eqn (2)):

$$\text{Dry weight loss} = (Wd_0 - Wd_t)/Wd_0 \times 100\%, \quad (2)$$

where Wd_0 represents the initial dry weight, and Wd_t represents the dry weight after degradation. Graphs were then plotted and analyzed in detail based on the above data.

Compressive strength assessment of hydrogels

The compressive strength of spherical CA and CA + AM hydrogels ($n = 3$ for each group) was evaluated. Prior to testing, the diameters of the hydrogels were measured using vernier calipers. The compression properties of the hydrogels were then assessed using a material tensile machine (Instron Mechanical Testing Systems, MA, USA) at a rate of 5 mm min^{-1}. This apparatus quantitatively measured the force exerted during the compression of the hydrogels.

Isolation, culture, and identification of bone marrow-derived macrophages (BMDM) and BMSC primary cells

BMDMs and third-generation BMSCs in a good growth state were used for induction culture, and cell identification was performed using flow cytometry for cell surface-specific markers[17] and immunofluorescence.[18]

Cytotoxicity assay

Fourth-generation BMDMs and BMSCs were co-cultured by adding 0.2%, 0.3%, 0.4%, 0.5% CA + AM, and CA at different solid contents. After implementing the above-described experimental design, the growth medium was removed, and the wells were washed thrice. Cell viability was measured using the CCK-8 assay kit, following the manufacturer's instructions. Absorbance at 450 nm was measured using an enzyme marker.[19]

Proliferation activity of cells

Fourth-generation BMSCs were collected and co-cultured with CA + AM and CA containing 0.5% solids. After a specific time point, the medium was discarded, and the cells were rinsed twice with PBS for 5 min each. Next, 1 μL of each propidium iodide (PI) (1000×) and calcein-AM (1000×) solution was added to PBS and mixed homogeneously. Then, 500 μL of the PI/calcein-AM solution was added to each well and incubated for 30 min at 37 °C while being protected from light. The green fluorescence of the inverted fluorescence microscope was used to observe live cells and red fluorescence was used to observe dead cells.

Alizarin Red S (ARS) staining and quantification

BMSCs were co-cultured with CA + AM and CA in a medium containing an osteogenic induction solution for 21 d. After a specific time point, the medium was removed, and the cells were washed thrice with PBS for 10 min each. The cells were fixed with paraformaldehyde (4%) for 30 min and washed thrice with PBS. Cells were stained by adding ARS staining solution (500 μL; Leagene, China) and placed in incubation at 37 °C for 30 min while being protected from light. Next, cells were removed from the ARS staining solution, washed twice with distilled water, and dried at room temperature before images were taken using a stereomicroscope. Finally, 500 μL of cetylpyrazine solution (10% w/v; Servicebio, China) was added to each well and incubated at 37 °C for 1 h, and the absorbance was measured at 562 nm using an enzyme marker.[20]

Polymerase chain reaction (PCR) for real-time fluorescence quantification

For the preparation of the reaction system, the primers, SYBR Green Mix, ddH_2O, and cDNA were prepared as a composite solution, uniformly mixed before being added to the PCR well plate. The reaction solution was then centrifuged at the bottom of a PCR plate at 37 °C for 1 min at 2000 rpm. Finally, a plate was set up, the program required for the reaction was implemented, and the fluorescence signal was recorded during the warm-up phase.

ALP staining

BMSCs were co-cultured with CA + AM and CA containing 0.5% solids in a medium containing an osteogenic induction solution for 7 and 14 days. Cells and images were obtained using a stereomicroscope.[21]

Western blot

Total protein was isolated from BMSCs using RIPA lysis buffer with a 1% protease inhibitor after 14 days. The protein concentrations were quantified using a BCA kit. After

electrophoresis and transfer membrane, the PVDF film was dried and prepared into a luminescent solution according to the manufacturer's instructions. An appropriate amount of luminescent solution was used to cover the PVDF film to be exposed to the luminometer for image acquisition, data processing, and analysis.

Establishment of a Sprague-Dawley (SD) rat mandibular anterior tooth extraction site preservation model

All animal procedures were performed in accordance with the Guidelines for Care and Use of Laboratory Animals of the Southern University of Science and Technology and experiments were approved by the Animal Ethics Committee of the Experimental Animal Center of Southern University of Science and Technology (Protocol no. SUSTech-JY202109009).

Exactly 30 healthy male SD rats with an average weight of 300–350 g were weighed before surgery. The 30 rats were randomly divided into three groups of ten rats each: Con, CA, and CA + AM groups, which were implanted with the corresponding materials.

Detection of hemostatic efficacy of tooth extraction wounds

The hemostasis procedure was divided into three groups. In the blank group, the bleeding was stopped at the extraction wound site using equal-weight sterile cotton balls (0.5 g), and the timing was conducted from the complete dislocation of the target tooth to the complete hemostasis of the extraction wound using a stopwatch. In the CA and CA + AM groups, the bleeding was stopped at the tooth wound site using a quantitative injection sample (0.5 g), the hemostatic time of five SD rats was obtained using a stopwatch, and detailed records were made. Under the same experimental conditions, the end weight of the hemostatic material used in the Con, CA, and CA + AM groups was measured, and the bleeding volume of the extraction wound was calculated by subtracting the initial weight from the end weight of the hemostatic material. Detailed records were made.

Analysis of extraction wound healing in SD rats by micro-computed tomography (micro-CT)

After week 4, the SD rats were euthanized, and the mandibles were fixed in 4% paraformaldehyde for 48 h and then immersed in PBS for micro-CT scanning and histological analysis. To evaluate osteogenesis in the extraction sockets of the SD rats, cross-sectional scans (Bruker Skyscan 1276, Massachusetts, USA) were performed using a microcomputer under the same experimental conditions (100 kV, 200 μA, 330 s). The images were processed and analyzed using CTAn software to measure the area and percentage of new bone formation in the SD rats. In addition, the percentage of new bone or bone volume/total volume ratio (BV/TV), bone mineral density (BMD), trabecular bone separation (Tb.Sp), and trabecular bone thickness (Tb.Th) were examined and analyzed separately for each group.

Micro-CT imaging analysis of alveolar bone regeneration in SD rats

To study the changes in alveolar bone quality and bone volume after tooth extraction in SD rats, micro-CT sections with certain representative coronal and lossy surfaces were selected from the three-dimensional images, and the sagittal sections were selected to include the proximal roots of the mandibular first molars and the top of the lingual alveolar crest of the incisors. The coronal section was located 1 mm before the lingual foramen; the red circle in Fig. 5c indicates the new bone area. The new bone area was expressed as the ratio of the new bone area to the alveolar area. To ensure the homogeneity of the measurement criteria, the image perspective of this experiment was based on a previous experimental method.[22]

Hematoxylin-eosin (H&E) and Masson's staining

Tissue samples were first dehydrated, then paraffinized, embedded in paraffin, and sliced into 4 μm thickness. The paraffin sections were rehydrated using xylene and a graded ethanol series. The slides were incubated with H&E and Masson's tri-chrome for 5 and 1 min, respectively.[21] Histological changes in the alveolar bone of SD rats after extraction of the left lower collar central incisor were photographed under the light microscope. The sections were examined using a pathology slide scanner (NanoZoomer S60; Hamamatsu Photonics, Japan).

Immunohistochemical (IHC) analysis

IHC analysis was conducted to assess the inflammatory response and bone repair efficacy of the hydrogels. Fixed tissue specimens were dehydrated in ethanol and embedded in paraffin. The expression levels of the specific detection index of M2 macrophage markers (iNOS, CD163) and bone regeneration indicators (Runx-2, OCN) were examined following standard procedures. Specimen slides were analyzed using a NanoZoomer S60 pathology slide scanner (Hamamatsu Photonics, Japan). To ensure objectivity, blinded evaluations of the slides were independently performed by two experienced pathologists.

Statistical analysis

All data were analyzed using GraphPad Prism 9.1 software and presented as the mean ± standard deviation (SD). Unpaired Student's *t*-tests and one-way analysis of variance (ANOVA) were applied for the statistical analysis, with $p < 0.05$ representing a statistical difference between the experimental data of each group. The notations used were: $*p < 0.05$, $**p < 0.01$, $***p < 0.001$, and $****p < 0.0001$.

Results

SEM and optical microscopy analyses

The CA enamelogenic protein composite hydrogel was successfully prepared. The naked eye view of the hydrogel, as shown in Fig. 1a, revealed good mechanical properties of the gel as follows: soft texture, spherical components that were

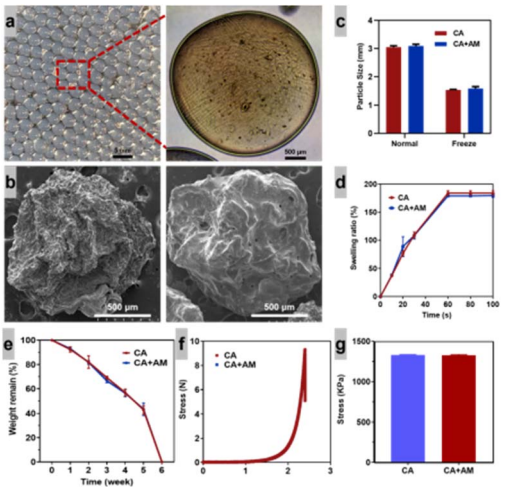

Fig. 1 Physical characterization of calcium alginate–amelogenin hydrogel (CA + AM) (a) visual observation of calcium alginate (CA) hydrogel. (b) Electron microscopic image of CA hydrogel and CA + AM. (c) Particle size comparison. (d) Swelling ratio. (e) Degradation ratio. (f and g) Compressive strength. Data represent mean ± standard deviation; ns: no significant difference, *p < 0.05, **p < 0.01, ***p < 0.001, and ****p < 0.0001.

transparent, uniform size (diameter of approximately 3 mm), closely arranged, contained water between them, translucent/colorless, and free of bubbles. The hydrogel exhibited distinct elasticity and strength, with a stable structure (not easy to break). Microscopic light microscopy of homogeneous, transparent, colorless, bubble-free, watery, morphologically, and structurally stable CA + AM with fluidity. Fig. 1b also shows that the structure of the CA composite did not change after AM addition, showing that the hydrogel has good structural stability. This demonstrates that the hydrogel has good structural stability and should not change its structure due to the compounding of other materials. According to Fig. 1c, the particle sizes of CA and CA + AM decreased before and after lyophilization, and there was no statistical difference between the two datasets. As shown from SEM imaging (Fig. 1b), the CA as well as the CA + AM, exhibited surface roughness, with a bumpy, wrinkled texture containing wrinkles of various sizes and shapes that were unevenly distributed on the surface.

Dissolution ratio, degradation ratio, and compression strength

Fig. 1d indicates that the CA has relatively fast swelling ratios both before and after the addition of composite AM, and the swelling process can be divided into two stages. In the first stage, the swelling ratio of hydrogels showed a linear increase during the swelling time of 0–60 s; in the second stage, the swelling of hydrogels reached swelling equilibrium during the swelling time of 60–120 s.

The results in Fig. 1e suggest that the degradation of CA and CA + AM was completed in 6 weeks. During weeks 1 to 5, 60% of the hydrogel mass degraded, and the degradation ratio was relatively stable; the remaining 40% degraded during weeks 5 to 6, and the degradation ratio increased significantly. Fig. 1f shows the results of the compressive strength tests of CA and CA + AM. When the displacement was 2.39 mm, the force on the hydrogel was 9 N, and the compressive strength of both CA and CA + AM was 1335 kPa, as shown in Fig. 1g. From the above experimental research results on hydrogel compression resistance, we concluded that CA + AM existed stably under a specific pressure strength and exhibited good performance in terms of physical and mechanical strength.

Cell culture, identification, and biocompatibility testing

Successfully induced macrophages were irregularly rounded or spindle-shaped, which perfectly matched the basic morphology of BMDMs after maturation.[23] Early growth was slow, showing clusters, and after fusion to 80%, they were cultured until the third generation; the mixed motley cells were on the low side, and the morphology of the cells was predominantly shuttle-shaped or flattened. The cells appeared to grow in a swirling pattern when fused, consistent with the morphology and growth characteristics of the primary cells of BMSCs.[24]

After taking cells with good growth viability and co-culturing them with CA or CA + AM gels of different solid contents for a specific time, the toxic effects of the gels on the cells were evaluated at specific time points to determine the solid content of the gels with relatively low biotoxicity to be used in subsequent experiments. The cell viability of BMSCs was significantly higher than the standard reference values on day 5 in all groups

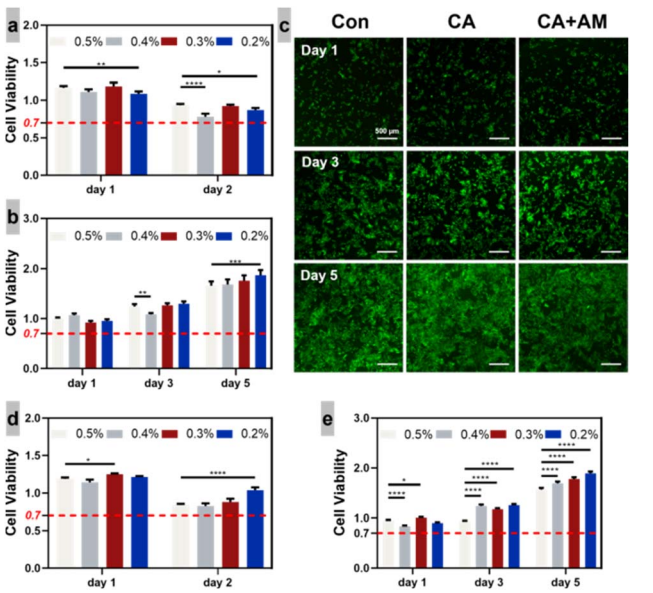

Fig. 2 Cell toxicity and proliferative activity at different concentrations of the hydrogel. (a) Bone marrow-derived macrophages (BMDMs) and (b) bone marrow mesenchymal stem cells (BMSCs) viability in the CA + AM group was performed and analyzed by CCK-8 assay. (c) Calcein/propidium iodide fluorescent staining of BMSCs proliferation. Green staining indicates living cells. (d) BMDMs and (e) BMSC viability in the CA group were performed and analyzed by CCK-8 assay. Data represent the mean ± standard deviation. ns: no significant difference, *p < 0.05, **p < 0.01, ***p < 0.001, and ****p < 0.0001.

co-cultured with CA + AM and CA (Fig. 2a and d), and the viability of BMDMs showed a significant decrease on day 2 in all groups co-cultured with CA but was higher than the standard reference values (Fig. 2b and e). Taken together, these results showed that CA + AM was non-toxic and had good biocompatibility. In addition, 0.5% solid content was neither toxic nor promoted bone proliferation; therefore, it was selected for further investigation of the role of CA + AM in promoting cell proliferation and osteogenesis.

At the beginning of the co-culture of BMSCs with CA + AM gel and 0.5% solid content, the green fluorescence in the CA group was significantly higher than that of the Con group. At the end of the culture period, the degree of green fluorescence in the CA group was significantly higher than that at the beginning of the culture period; however, there was almost no apparent red fluorescence throughout the culture period (Fig. 2c), indicating that the BMSCs had good proliferation activity at 0.5% solid content of CA.

BMDMs polarization

As shown in Fig. 3a, the CA + AM group demonstrated significant stimulation of macrophage polarization toward M2 compared to the CA group, indicating that the CA + AM gel exhibited an inhibitory effect on inflammation.

ARS and ALP staining, osteogenesis-related genes, and protein testing

BMSCs and gels were co-cultured for 7 and 14 d, and the experimental results showed that on day 7 of culturing, ALP staining did not indicate statistically significant differences between the groups (Fig. 3b). However, the ALP activity in the CA + AM group was significantly higher than that in the Con group on day 14 of culturing, indicating that the CA + AM group exhibited a stronger osteogenesis-promoting effect.

ARS staining and quantitative analysis (Fig. 3c) showed that the CA + AM group exhibited a more significant effect on promoting calcium deposition than did the CA and Con groups; however, there was no statistically significant difference between the CA hydrogel and Con groups. The gene expression of runt-related transcription factor (Runx)-2, Osterix, ALP, osteocalcin (OCN), collagen (Col)-1, and bone morphogenic protein (BMP)-2 in the CA + AM group was significantly different from that in the Con group (Fig. 3d), indicating that the CA + AM gel had a high ability to accelerate osteogenesis. Western blot detection of Col-1, OCN, ALP, Runx-2, and GAPDH proteins was consistent with the expression trends of osteogenic-related proteins.

Establishment of a preservation model, *in vivo* hemostasis, and osteogenic evaluation of mandibular anterior extraction sites

A model of mandibular anterior tooth extraction site preservation was successfully constructed (Fig. 4a). The results of the bleeding time (Fig. 4b) showed that the bleeding time in the CA + AM group was 5–7% of that in the Con group, indicating that the CA + AM group completed hemostasis in a relatively short

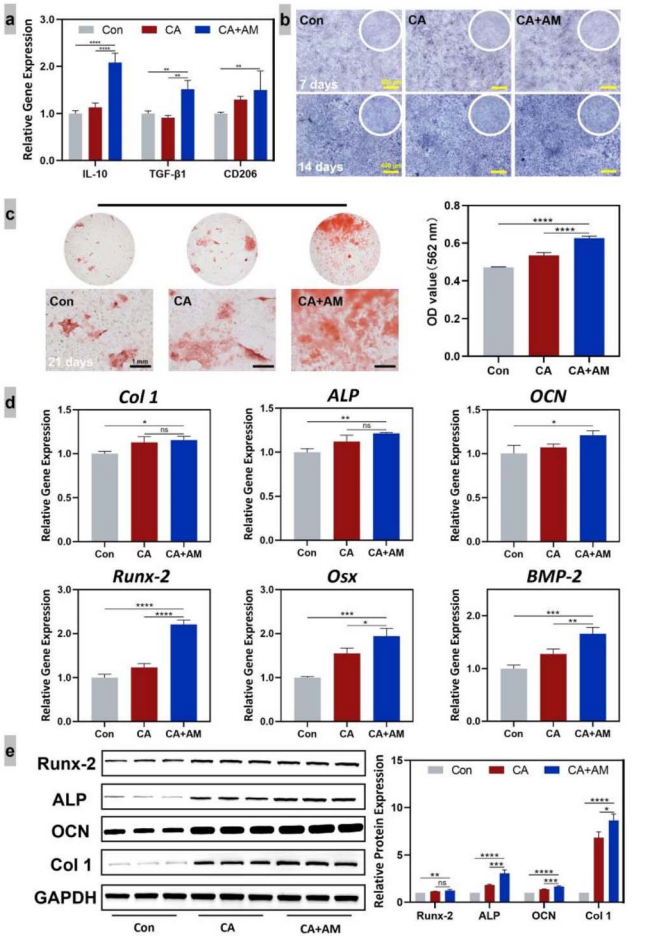

Fig. 3 Effect of CA + AM on macrophage morphology and expression of inflammatory and osteogenic genes and proteins. (a) CA + AM promotes the polarization of macrophages to M2. (b) Alkaline phosphatase staining. (c) Alizarin red staining and quantitative analysis. (d) Expression of osteogenesis-associated genes. (e) Quantitative analysis and expression of osteogenesis-related proteins. Data represent mean ± standard deviation. ns: no significant difference, *p < 0.05, **p < 0.01, ***p < 0.001, and ****p < 0.0001.

time, with reduced bleeding in the extraction wound. Experimental results (Fig. 4c) showed that bleeding in the CA + AM group was significantly less than in the Con group. The data showed that bleeding in the CA + AM group was only 20–30% of that in the Con group, indicating that bleeding from the extraction wound was substantially reduced.

By observing and analyzing the resorption of the alveolar crest width (Fig. 5a, yellow lines) and height (Fig. 5b, red lines), the extent of alveolar crest resorption in the CA + AM group was significantly lower than that in the Con group, measuring approximately 20–30% of the resorption observed in the Con group.

Furthermore, the experimental results shown in Fig. 5a reveal that the alveolar ridge resorption ratio on the labial and lingual sides of the CA + AM group was significantly lower than that of the Con group. The data showed that the alveolar ridge resorption ratio on the labial and lingual sides of the CA + AM group was 40–50% of that of the Con group, illustrating that CA

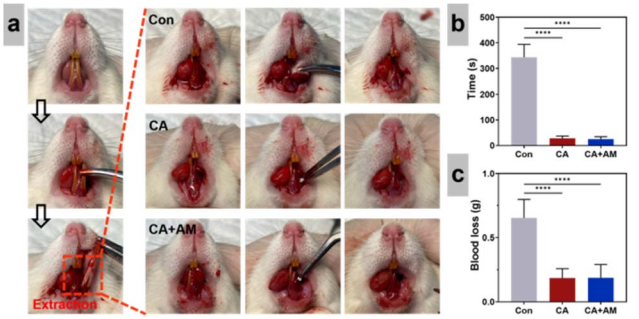

Fig. 4 Animal model construction. Dental extraction of the lower central incisor in Sprague Dawley rats to evaluate the effects of different treatments on the (a) extraction socket healing, (b) bleeding time, and (c) amount of blood loss. *p < 0.05, **p < 0.01, ***p < 0.001, and ****p < 0.0001.

+ AM exhibits good physical properties and can play a supporting role for the extraction sockets in the early stage of tooth extraction.

In addition, the data suggest that CA + AM can promote the formation of new bone, reduce resorption of the alveolar ridge, and prevent crest resorption and invagination.[25] By observing and analyzing the coronal (Fig. 5c, red circles) and lost (Fig. 5d, red triangles) positions of the sockets 28 d after extraction, it was noticeable that new bone tissue filled almost the entire socket of CA + AM-treated rats, with the osteogenic area being approximately 1.8 times that of the Con group. The experimental results showed that a large amount of new bone appeared in the extraction fossa of the CA + AM group, which is further evidence that CA + AM can promote bone tissue with great advantage.

The results also showed a large amount of new bone formation in the extraction fossa of the CA + AM group (Fig. 6a), and the amount of new bone was greater than that in the Con, CA, and CA + AM. At the same time, the experimental results revealed (Fig. 6a) that the amount of new bone formation was significantly higher in the CA + AM group at day 28 than at day 7 after extraction. The BMD of the new bone in the CA + AM group was significantly higher than in the other groups on days 7 and 28 after tooth extraction (Fig. 6b). The BMD and BV/TV ratios were 1.71 and 2.64 times higher in the CA + AM group than in the Con group on day 7 and 1.41 and 1.78 times higher on day 28, respectively (Fig. 6b and c). There was no significant difference in Tb.Sp in the CA + AM group; however, Tb.Th was significantly greater than that in the Con group (Fig. 6d and e). The tissue of the newly formed bone had sufficient trabecular thickness. The above experimental data demonstrate that CA possesses good biocompatibility, can exist stably in the extraction sockets, and can promote bone-tissue regeneration.

H&E staining of the hard tissues of the extraction wound was performed on days 7 and 28 after extraction to evaluate and analyze the new bone tissue at a deeper level (Fig. 7a). On day 7, the results showed that the scaffold material in the CA + AM group was degraded and replaced by new bone tissue (black arrow), with significantly more new bone tissue in the CA + AM group and less fibrous tissue (green arrow) than in the Con group. After observing the results of staining on day 28 after the extraction, a large amount of new bone tissue was formed in the CA + AM group, and there was almost no fibrous tissue around the new bone tissue (green arrow); however, a specific amount of new bone tissue was deposited in the central area of the defect of the extraction socket in the Con group. In addition, the percentage of new bone tissue in the extraction sockets was

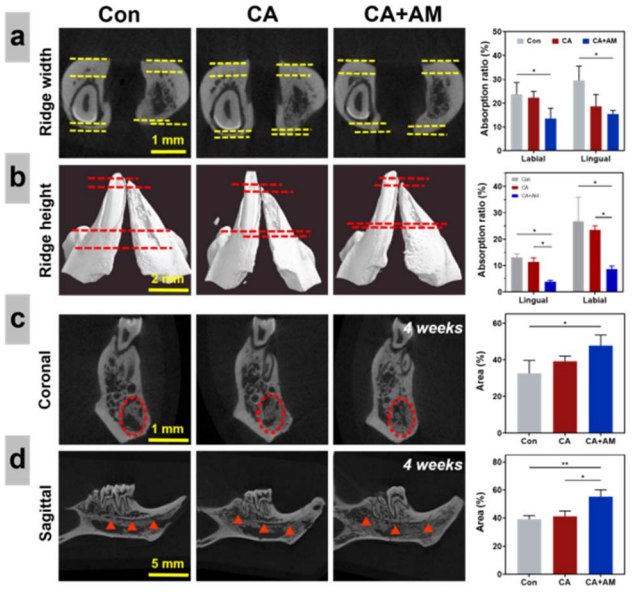

Fig. 5 Degree of resorption of the alveolar ridge after tooth extraction trauma. (a and b) Absorption of the width and height of the sagittal alveolar ridge. (c and d) Osteogenesis in the socket 28 days after tooth extraction. *p < 0.05, **p < 0.01, ***p < 0.001, and ****p < 0.0001.

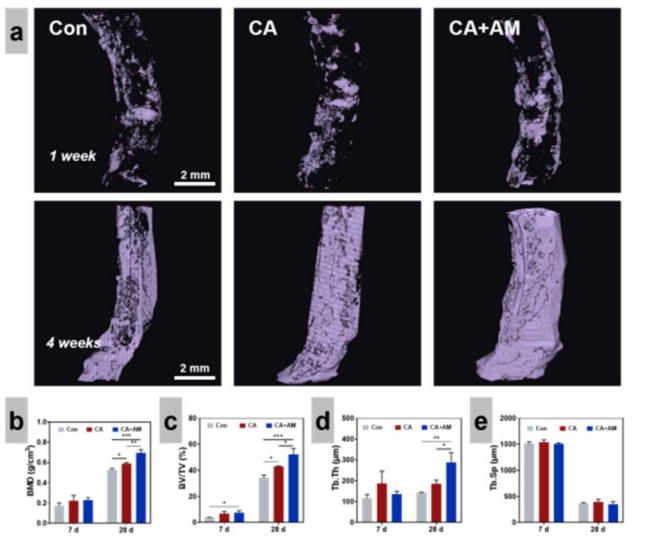

Fig. 6 New bone formation in the extraction sockets of Sprague-Dawley rats. (a) New bone formation; (b) bone mineral density (BMD); (c) bone volume/total volume (BV/TV); (d) trabecular thickness (Tb.Th), and (e) trabecular separation (Tb.Sp) in the tooth-extracted socket at the indicated time points. Error bars represent the mean ± standard deviation. *p < 0.05, **p < 0.01, ***p < 0.001, and ****p < 0.0001.

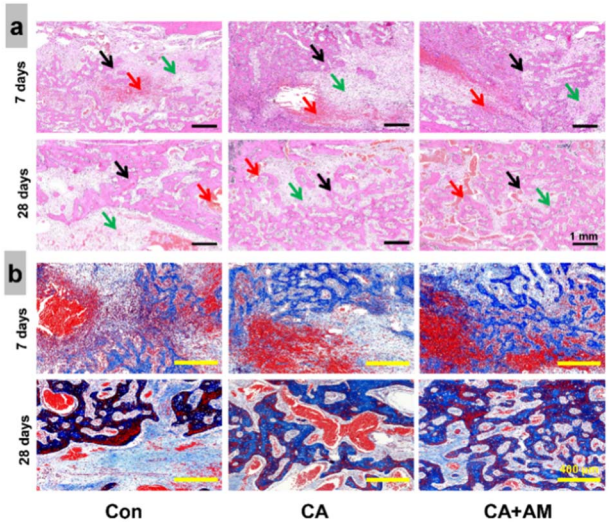

Fig. 7 Histological staining in the extraction sockets of Sprague-Dawley rats. (a) H&E staining sections on days 7 and 28 after tooth extraction. Black, green, and red arrows indicate new bone, fibrous tissue, and blood clots, respectively. (b) Masson's staining sections on days 7 and 28. Blue and red colours indicate fibrous tissue and mature bone tissue, respectively.

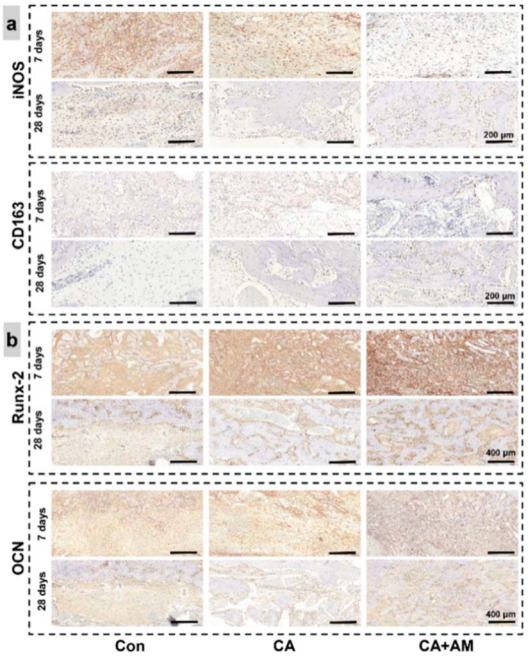

Fig. 8 IHC analysis in the extraction sockets of Sprague-Dawley rats. (a) The expression of markers (iNOS and CD163) of BMDM polarization on days 7 and 28. (b) The expression of osteogenic markers (runx-2 and OCN) after 7 and 28 days.

significantly lower than in the CA + AM group. The above experimental results indicate that the CA + AM group could coexist with the host without significant inflammation or immune response, which provided a suitable *in vivo* environment for osteoblast proliferation and differentiation.

Masson's staining (Fig. 7b) revealed a remarkable presence of fibrous tissue (blue color) within the extraction sockets across all groups at the four-week mark. Notably, this fibrous tissue was interspersed with remnants of degraded gel material.

However, there were more ossification centers in the gel group than those in the control group. Furthermore, the CA + AM group displayed a larger area of mature bone tissue (stained red) than that of the other groups. Additionally, the CA group demonstrated a greater extent of mature bone formation than that demonstrated by the control group. These findings are corroborated by previous observations.

IHC revealed a marked increase in CD163+ cells, alongside a decrease in iNOS+ cells in the CA + AM group (Fig. 8a). This shift may be attributed to BMDM polarization, potentially induced by the sustained release of AM from the hydrogels. Additionally, the expression levels of OCN and Runx-2 (Fig. 8b) are indicative of osteogenic activity. The results suggested that there was a large positive cell expression in the gel, which was higher in the CA + AM group, further corroborating the osteogenic capacity of the gel under *in vivo* conditions.

Discussion

In this study, we successfully synthesized a CA + AM hydrogel and thoroughly evaluated its swelling properties, degradation ratio, compression strength, effect on the polarization direction of macrophages, and both hemostatic and osteogenic efficacies.

For bone regeneration, it is critical that bio-scaffold materials not only exhibit biocompatibility and biodegradability but also possess robust mechanical properties, facilitate osteoconduction and induction, and, most importantly, support stem cell infiltration and proliferation for new bone formation.[13–15] However, bio-scaffolds often encounter issues like immunological rejection and structural instability. Addressing this, our study aimed to develop a novel scaffold material that can cater to a broad patient spectrum. Current findings suggest that enamel can induce the regeneration of periodontal support tissues (gingival, periodontal, osseous, and alveolar bone);[7–9] however, AM tends to degrade rapidly in periodontal tissue defect sites.[11,12] To mitigate this, we incorporated AM into a drug-loaded CA hydrogel, achieving promising results in addressing this challenge. As a bone-tissue-engineering scaffold material, CA hydrogels promote the generation of new tissues, which requires a certain degree of degradation during the process of new tissue generation. Degradability, an essential property of bioactive materials, significantly impacts tissue regeneration at the defect sites. Earlier studies have reported that rapidly degrading hydrogels can significantly improve the extent and quality of tissue regeneration.[26] The results of hydrogel degradation experiments showed in this study that hydrogels maintained relatively stable degradability in the early stages and exhibited a high degradation ratio in the later stages, which enabled them to provide adequate and stable skeletal support in the early stages of cell growth. However, they degraded rapidly after tissue growth was complete; therefore, we infer that tissue regeneration should be optimal when the ratio of hydrogel degradation matches that of

cytoplasmic matrix formation. Meinel *et al.*[27] showed that hydrogels play a crucial role as scaffolding materials in the processes of cellular value addition and new tissue differentiation and that hydrogels degrade rapidly if cells do not deposit sufficient amounts of extracellular matrix to replace the degrading hydrogels. Before the hydrogel degrades rapidly, it tends to collapse the collagen scaffold, which affects tissue generation. High-strength hydrogels are vital in promoting soft-tissue repair, bone-tissue regeneration, and wound healing. Experimental studies on the compressive properties of hydrogels have shown that CA + AM is stable at a certain pressure and exhibits good performance in terms of physical and mechanical strength. Stubbe *et al.*[28] experimentally demonstrated that CA hydrogels possess good biocompatibility and that chondrocytes can be cultured in CA hydrogels for a long time. Experimental studies have shown that CA accelerates tissue healing and regeneration in wounds.[29]

In this study, CA + AM caused less bleeding and required less time to stop bleeding than the Con group. Due to their high swelling ratio, CA hydrogels can absorb exudate from wounds; however, an increase in calcium ion concentration is the leading cause of platelet activation, promoting blood clotting.[30] Moreover, Ca^{2+} can be mobilized by various secondary messengers that act on specific receptors and channels, such as inositol triphosphate receptors, ryanodine receptors, and dual pore channels, which contribute to blood coagulation channels.[31,32] A previous report suggested that injectable hydrogel systems may require less healing time than conventional stents.[33] The bleeding experiments showed that CA + AM possesses adhesive and physical plugging properties that significantly reduce wound bleeding and infection.

The role of CA + AM in promoting osteogenesis was explored by examining the expression of osteogenesis-related genes and proteins in BMSCs. In the early stages of osteogenesis, Runx-2 could bind to osteoblasts while promoting the differentiation of BMSCs into osteoblasts to regulate the expression of osteogenic factors such as BSP and OPN.[34] However, excessively high expression of ALP can promote the differentiation of pro-osteoblasts into mature osteoblasts, accelerating bone matrix formation and mineralization.[35] Osterix, a downstream gene in the Runx-2 signaling pathway, significantly regulates the proliferation and differentiation of osteoblasts and bone matrix production.[36] OCN and Col-1 regulate osteogenesis, bone matrix mineralization, and calcium ion stabilization.[37] BMP-2 plays a role in the recruitment and differentiation of undifferentiated mesenchymal and osteoblastic cells. It promotes the differentiation of Runx-2, Osterix, ALP, OCN, Col-1, and BMP-2 as essential and landmark substances in the osteogenesis process, as was shown to be expressed in the CA + AM group compared with the Con group. The experimental data indicate that the CA + AM gel had a high affinity to accelerate osteogenesis, and the expression results of Col-1, OCN, ALP, Runx-2, and GAPDH proteins detected by western blot were consistent with the expression trends of osteogenic factor genes. The improved osteogenic ability of CA + AM may be related to the unique pore-containing structure of the material. The same trend can be seen in IHC (Fig. 8b). As a biodegradable bioactive material with a loose porous structure and high permeability, CA + AM exhibits a strong cell-carrying capacity for oxygen exchange, cell migration, and the diffusion of nutrients.[38]

Width and height are the most direct indicators of changes in alveolar crest bone density; however, changes in labial and lingual alveolar crest lengths are essential for measuring the alveolar crest resorption ratio.[25,39] Three-dimensional scanning and analysis of the extraction wound and surrounding alveolar bone in SD rats using micro-CT showed that CA + AM exhibited good physical properties, which can support the extraction socket in the early stages of extraction, promote new bone formation, reduce alveolar ridge resorption, and prevent the resorption and ingrowth of the alveolar ridge.[25]

In organisms, BMDMs are involved in the onset, development, and digestion of inflammation. At different stages of the inflammatory response, BMDMs exhibit different phenotypes.[40] BMDMs have at least two different polarizations, M1-type polarization and M2-type polarization.[40,41] M1-type polarization is characterized by elevated levels of proinflammatory cytokines and antimicrobial and tumoricidal activities, and M2-type polarization is associated with immunosuppression and tissue repair.[40,41] The characteristic surface markers of M2-type BMDMs are interleukin-10, transforming growth factor (TGF)-β1, and mannose receptor (CD206).[42] In this study, we investigated the regulatory effect of CA + AM on BMDMs by examining its effect on the expression of BMDM-related inflammatory factors after co-culturing with BMDMs. The experimental results showed that CA + AM could regulate the polarization of BMDMs towards M2 and had significant anti-inflammatory properties, which can be observed in the same trend in IHC (Fig. 8a); subsequently, it could absorb inflammatory exudates and reduce infections.

However, the pathways through which CA + AM regulates BMDMs remain unclear and require further investigation. This study showed that CA + AM possesses unique biocompatibility, can reduce wound infection, promote wound healing and alveolar bone regeneration, and can be used as an alveolar bone restoration material.

Conclusions

CA + AM was prepared using hybrid and ionic cross-linking methods and tested to reveal good swelling properties, degradability, and physical and mechanical properties. The composite hydrogel has good biosafety, and its degradation products are non-toxic and can coexist with organisms. According to osteogenesis-related experimental results, the hydrogel promoted osteoblast mineralization, osteogenesis-related genes, and osteogenesis-related protein expression, thereby efficiently promoting osteogenesis. In addition, the high expression of macrophage-associated inflammatory factors interleukin-10, TGF-β1, and CD206 after co-culture of the hydrogel with macrophages indicated that it could promote macrophage polarization towards M2, indicating anti-inflammatory properties that may promote tissue healing of near wounds and prevent wound infection.

Author contributions

Investigation and validation, T. Z., C. Y., G. H. and H. L.; formal analysis, T. Z., and L. C.; writing – original draft, T. Z. and C. Y.; visualization, L. C., C. Y., and G. H.; resources, Z. C., Y. H., W. S. and J. Z.; conceptualization, methodology, Z. C., T. Z., L. C. and H. S; writing – review & editing, supervision, W. S. and J. Z.; funding acquisition, project administration, L. C., H. S., and Y. H. All authors have read and agreed to the published version of the manuscript.

Conflicts of interest

There are no conflicts to declare.

Acknowledgements

This work was supported by the Shenzhen Science and Technology Program [grant no. JCYJ20190814114605162] and [grant no. KCXFZ20230731100659001] and [grant no. SGDX20201103095600002] and the Guangdong Basic and Applied Basic Research Foundation [grant no. 2019A1515110511].

Notes and references

1 X. Wang, C. Li, T. Q. He, W. H. Zheng, W. Liu, Y. Y. Zhang, X. L. Chen, Y. Q. Zhou, C. Y. Shui, Y. D. Ning, Y. C. Cai, J. Jiang, R. H. Sun and W. Wang, *Zhonghua Er Bi Yan Hou Tou Jing Wai Ke Za Zhi*, 2021, **56**, 89–92.
2 J. Guo, H. Yao, X. Li, L. Chang, Z. Wang, W. Zhu, Y. Su, L. Qin and J. Xu, *Bioact. Mater.*, 2023, **21**, 175–193.
3 M. Filippi, G. Born, M. Chaaban and A. Scherberich, *Front. Bioeng. Biotechnol.*, 2020, **8**, 474.
4 H. Yao, J. Guo, W. Zhu, Y. Su, W. Tong, L. Zheng, L. Chang, X. Wang, Y. Lai, L. Qin and J. Xu, *Pharmaceutics*, 2022, 14.
5 Q. Feng, J. Xu, K. Zhang, H. Yao, N. Zheng and L. Zheng, *ACS Cent. Sci.*, 2019, **5**, 440–450.
6 J. Sun and H. Tan, *Materials*, 2013, **6**, 1285–1309.
7 B. Urzua, R. Ahumada-Ossandon, D. Casa-Weisser, M. E. Franco-Martinez and A. Ortega-Pinto, *J. Dent. Sci.*, 2021, **16**, 7–14.
8 S. Li, S. Ge and P. Yang, *J. Periodontal Res.*, 2015, **50**, 846–854.
9 N. Y. Shin, H. Yamazaki, E. Beniash, X. Yang, S. S. Margolis, M. K. Pugach, J. P. Simmer and H. C. Margolis, *J. Biol. Chem.*, 2020, **295**, 1943–1959.
10 K. Yamamichi, T. Fukuda, T. Sanui, K. Toyoda, U. Tanaka, Y. Nakao, K. Yotsumoto, H. Yamato, T. Taketomi, T. Uchiumi and F. Nishimura, *Arch. Oral Biol.*, 2017, **83**, 241–251.
11 T. Jiang, F. Liu, W. G. Wang, X. Jiang, X. Wen, K. J. Hu and Y. Xue, *PLoS One*, 2017, **12**, e0169857.
12 L. Zhu, H. Liu, H. E. Witkowska, Y. Huang, K. Tanimoto and W. Li, *Front. Physiol.*, 2014, **5**, 268.
13 R. Agarwal and A. J. Garcia, *Adv. Drug Delivery Rev.*, 2015, **94**, 53–62.
14 J. Barros, M. P. Ferraz, J. Azeredo, M. H. Fernandes, P. S. Gomes and F. J. Monteiro, *Mater. Sci. Eng., C*, 2019, **105**, 109985.
15 X. Yu, X. Tang, S. V. Gohil and C. T. Laurencin, *Adv. Healthcare Mater.*, 2015, **4**, 1268–1285.
16 N. B. Guerra, G. Sant'Ana Pegorin, M. H. Boratto, N. R. de Barros, C. F. de Oliveira Graeff and R. D. Herculano, *Mater. Sci. Eng., C*, 2021, **126**, 112126.
17 A. Mily, S. Kalsum, M. G. Loreti, R. S. Rekha, J. R. Muvva, M. Lourda and S. Brighenti, *J. Visualized Exp.*, 2020, **163**, e61807.
18 K. Im, S. Mareninov, M. F. P. Diaz and W. H. Yong, *Methods Mol. Biol.*, 2019, **1897**, 299–311.
19 M. Y. Li, X. L. Zhu, B. X. Zhao, L. Shi, W. Wang, W. Hu, S. L. Qin, B. H. Chen, P. H. Zhou, B. Qiu, Y. Gao and B. L. Liu, *Cell Death Dis.*, 2019, **10**, 489.
20 C. M. Giacomino, J. A. Wealleans, N. Kuhn and A. Diogenes, *J. Endod.*, 2019, **45**, 51–56.
21 Y. C. Ryu, D. H. Lee, J. Shim, J. Park, Y. R. Kim and S. Choi, *Br. J. Pharmacol.*, 2021, **178**, 2533–2546.
22 X. Xu, Z. Gu, X. Chen, C. Shi, C. Liu, M. Liu, L. Wang, M. Sun, K. Zhang, Q. Liu, Y. Shen, C. Lin, B. Yang and H. Sun, *Acta Biomater.*, 2019, **86**, 235–246.
23 X. Cao, G. K. Yakala, F. E. van den Hil, A. Cochrane, C. L. Mummery and V. V. Orlova, *Stem Cell Rep.*, 2019, **12**, 1282–1297.
24 W. Wang and B. Wang, *Int. Immunopharmacol.*, 2021, **98**, 107821.
25 Y. Pan, Y. Zhao, R. Kuang, H. Liu, D. Sun, T. Mao, K. Jiang, X. Yang, N. Watanabe, K. H. Mayo, Q. Lin and J. Li, *Mater. Sci. Eng., C*, 2020, **116**, 111158.
26 M. J. Mahoney and K. S. Anseth, *Biomaterials*, 2006, **27**, 2265–2274.
27 L. Meinel, S. Hofmann, V. Karageorgiou, L. Zichner, R. Langer, D. Kaplan and G. Vunjak-Novakovic, *Biotechnol. Bioeng.*, 2004, **88**, 379–391.
28 B. Stubbe, A. Mignon, H. Declercq, S. Van Vlierberghe and P. Dubruel, *Macromol. Biosci.*, 2019, **19**, e1900123.
29 G. Chen, Y. Zhou, J. Dai, S. Yan, W. Miao and L. Ren, *Int. J. Biol. Macromol.*, 2022, **216**, 686–697.
30 M. Ido, S. Kato, H. Ogawa, K. Hayashi, Y. Komada, X. L. Zhang, M. Sakurai and K. Suzuki, *Thromb. Haemostasis*, 1996, **76**, 439–443.
31 K. Mizuno, K. Kurokawa and S. Ohkuma, *J. Pharmacol. Sci.*, 2013, **123**, 306–311.
32 A. J. Morgan and A. Galione, *Bioessays*, 2014, **36**, 173–183.
33 X. Zhao, H. Wu, B. Guo, R. Dong, Y. Qiu and P. X. Ma, *Biomaterials*, 2017, **122**, 34–47.
34 Q. Wang, X. Xie, D. Zhang, F. Mao, S. Wang and Y. Liao, *Bioengineered*, 2022, **13**, 431–439.
35 S. Vimalraj, *Gene*, 2020, **754**, 144855.
36 Y. Xu, Y. Jin, F. Hong, Y. Ma, J. Yang, Y. Tang, Z. Zhu, J. Wu, Q. Bao, L. Li, B. Yao, D. Li and C. Ma, *J. Cell. Mol. Med.*, 2021, **25**, 5025–5037.
37 P. Cai, Y. Lu, Z. Yin, X. Wang, X. Zhou and Z. Li, *Aging*, 2021, **13**, 17370–17379.

38 D. Chimene, R. Kaunas and A. K. Gaharwar, *Adv. Mater.*, 2020, **32**, e1902026.
39 Y. Arai, K. Aoki, Y. Shimizu, Y. Tabata, T. Ono, R. Murali, S. Mise-Omata and N. Wakabayashi, *Eur. J. Pharmacol.*, 2016, **782**, 89–97.
40 F. O. Martinez, A. Sica, A. Mantovani and M. Locati, *Front. Biosci.*, 2008, **13**, 453–461.
41 A. Mantovani, S. Sozzani, M. Locati, P. Allavena and A. Sica, *Trends Immunol.*, 2002, **23**, 549–555.
42 R. Lv, Q. Bao and Y. Li, *Mol. Med. Rep.*, 2017, **16**, 9111–9119; B. Yang, J. Song, Y. Jiang, M. Li, J. Wei, J. Qin, W. Peng, F. L. Lasaosa, Y. He, H. Mao, J. Yang and Z. Gu, *ACS Appl. Mater. Interfaces*, 2020, **12**, 57782–57797.